Catalysis Today 175 (2011) 515–523

Contents lists available at ScienceDirect

Catalysis Today

journal homepage: www.elsevier.com/locate/cattod

# Microemulsion and incipient wetness prepared Rh-based catalyst for diesel reforming

Xanthias Karatzas[a,*], Kjell Jansson[b], Jazaer Dawody[c], Roberto Lanza[a], Lars J. Pettersson[a]

[a] KTH – Royal Institute of Technology, Department of Chemical Engineering and Technology, Teknikringen 42, SE-100 44 Stockholm, Sweden
[b] Stockholm University, Arrhenius Laboratory, Department of Materials and Environmental Chemistry, SE-106 91 Stockholm, Sweden
[c] PowerCell Sweden AB, Ruskvädersgatan 12, SE-418 34 Göteborg, Sweden

ARTICLE INFO

*Article history:*
Received 15 October 2010
Received in revised form 6 February 2011
Accepted 28 February 2011
Available online 3 April 2011

*Keywords:*
Autothermal reforming
Diesel
Incipient wetness
Platinum
Reverse microemulsion
Rhodium

ABSTRACT

The role of the catalyst preparation technique was investigated for diesel reforming. Reverse microemulsion (ME) and incipient wetness (IW) techniques were used for the preparation of Rh-based monolithic catalysts that were employed for hydrogen generation of low-sulfur diesel via autothermal reforming (ATR). The washcoat of the tested catalysts consisted of 0.5 wt% Rh, 1 wt% Rh, and 1:1 wt% Rh:Pt supported on γ-alumina. All washcoats were deposited on 400 cpsi cordierite monoliths. The reaction condition was $T_{feed}$ = 650 °C, $H_2O/C \sim 2.5$, $O_2/C \sim 0.49$, TOS = 3 h, GHSV ~ 13 000 $h^{-1}$ and $P$ = 1 atm. Fresh and aged powder samples of the catalyst were characterized by $N_2$-BET, $H_2$ chemisorption, XRD, $H_2$-TPR, $O_2$-TPO and TEM.

The activity results established that Rh and RhPt formulations, prepared by ME and IW, are highly active for ATR of diesel where fuel conversions above 92% were obtained. FTIR and NDIR analysis also showed that the highest formation of ethylene was found in the product gas stream from the bimetallic samples indicating that $RhPt/Al_2O_3$ is less resistant towards carbon deposition. The latter observation was confirmed by $O_2$-TPO analysis of the aged samples where high loads of coke were found both on the active metals and on the support. Interestingly, these effects were less significant on the ME samples.

The characterization results clearly showed differences in morphology between the ME and the IW samples. $N_2$-BET analysis showed that higher surface area, ~268–285 $m^2/g$, was obtained with the ME samples. Also, $H_2$ chemisorption analysis showed that the rhodium dispersion was ~10% higher for the ME samples (H/Rh ~ 60–66%). XRD analysis showed that crystalline phases of γ-alumina were present on all samples. The diffractograms also showed small traces of metallic Pt (~16–30 nm) in the bimetallic samples. $H_2$-TPR analysis, showed peaks ascribed to bulk rhodium oxides and rhodium aluminates. It was also noted that the addition of Pt on the support lowered the reducibility of the different rhodium species. TEM analysis performed on the fresh and aged ME and IW bimetallic samples showed mainly $Rh_xPt_{1-x}$ alloys with an average particle size of ~20–50 nm were present on the alumina support. Also, for the aged samples, no sintering effects were noted. Furthermore, rhodium was found to switch oxidation state from e.g. $Rh^{3+}$ to $Rh^0$ while Pt remained in the metallic state.



## 1. Introduction

Due to stringent legislation concerning idling emissions of $NO_x$, CO and HC during the last few years, particularly in the US [1–3], fuel cell auxiliary power units (FC-APU) has emerged as a very promising technology for heavy-duty diesel trucks [3,4]. Idling emissions are generated when the trucks are at standstill while the engine is still in use. Idling typically occurs when drivers utilize the vehicles' electronic comfort units (e.g. A/C, radio, TV, computer) e.g. during cargo off-loading as well as spending overnight at rest-stops [3,4]. Statistics have shown that diesel trucks operate in the idling mode during 20–40% of total operating time [4,5]. This is detrimental as both the truck drivers' health and diesel engine life-time are jeopardized, at risk of being shortened [2–5]. Several articles have shown the potential of using 5–10 $kW_e$ polymer-electrolyte fuel cell (PEFC) based, hydrogen-fed, FC-APU units to provide the necessary electricity needed during idling [6–8]. In this case, the fuel-cell utilizes hydrogen, along with air, to generate electricity forming steam as a by-product. Total life-cycle emission predictions have shown that pollutants from FC-APU will be 99% lower compared to idle operation of diesel engines [9]. Besides lower emissions, other benefits with an FC-APU utility are: portability, meaning it can be directly integrated with the set-up of the diesel trucks; silent operation; and also a high overall energy efficiency, up to 36% can be achieved [3,6,8]. In an FC-APU, the hydrogen storage problem is circumvented as hydrogen is generated onboard

* Corresponding author. Tel.: +46 87908236.
*E-mail address:* xanthias@kth.se (X. Karatzas).

0920-5861/$ – see front matter © 2011 Elsevier B.V. All rights reserved.
doi:10.1016/j.cattod.2011.02.042

from diesel (energy density ~38.6 MJ/dm$^3$) by a catalytic reformer. The hydrogen yield can be further improved by sequential high- and low-temperature water-gas-shift (WGS) units [10]. Different concepts for reactor design of onboard catalytic diesel reformers have been published both in the micro- and full-scale [10,11]. Most of these reactors are based on the autothermal reforming (ATR) process technology, which is a dynamic and energy-efficient process capable of handling the frequent start-ups and shutdowns occurring both during transient and steady state operation of the diesel trucks. Furthermore, most of the reactors employ washcoated monoliths as catalyst. These catalytic systems have been proven to be ideal for automobile systems both in the past 30 years and in present e.g. in the use of exhaust gas cleaning of CO, HC and $NO_x$ [12].

In recent years many studies have been performed focusing on the optimization of the washcoat composition of the diesel reforming monolithic catalyst. Base metals such as Ni, Co and Fe have been tested and shown high activity and selectivity for ATR; however the durability and stability of these materials are poor due to catalyst deactivation e.g. volatilization of active metal particles, sintering effects and coke deposition on active sites [13,14]. Low loadings of rhodium and rhodium–platinum formulations have proven to be very active for diesel reforming [15,16]. These noble metals are both mechanically and thermally stable at the high reaction temperatures that are carried out for diesel reforming, ~650–900 °C [6,10,17]. The noble metals are also capable of handling both the oxidative and reductive environment occurring during ATR, and are also very resistant against deactivation mechanisms e.g. sulfur poisoning and carbon deposition [15,18]. A variety of supports have been documented and used for the Rh-based catalyst e.g. alumina, zirconia, ceria–zirconia, pyrochlores and magnesium oxide, among others [6,15–17,19–21]. Most of these catalysts have been prepared by conventional methods. A typical example is the incipient wetness (IW) method. In this case, the support material is impregnated by an aqueous solution of the Rh metal precursor, often nitrate solutions, in order to fill up the pores of the support. The impregnated material is then dried, calcined and reduced in order for the crystalline metal particles to be formed within the pores of the support. This method is easy and straight forward to implement. On the other hand, the particle size distribution is often broad since it is often influenced by the pore thickness of the support. Also, the dispersion can be low since the particle positioning of the impregnated metals is stochastic which may lead to particle agglomeration [22–24]. A preparation method that has attracted increasing interest during last decade is the microemulsion (ME) method [22–24]. The method generally involves using one or two thermodynamically stable solutions of water/oil emulsions blended with a reducing agent e.g. hydrogen, hydrazine or ammonia. In this case, the formation of the crystalline metal particles takes place already at room temperature in the microemulsion, after the addition of a reducing agent. Unlike IW, the particle size distribution does not rely on the pore thickness of the support but rather on the nature of the microemulsions employed. The particle size can be controlled e.g. by varying the water-to-surfactant ratio. Hence, smaller nano-sized particles can be generated with narrow size distribution. Lately, ME prepared noble-metal based catalysts have with promising results been tested for high temperature application such as partial oxidation of methane [25,26]. However, limited studies can be found in the literature where noble metal ME catalysts have been used for diesel reforming. Hence, it is interesting to find out the activity, selectivity, stability and durability of these particular catalysts.

In this study, ATR of low sulfur diesel was tested at bench scale to detect differences in activity for IW and ME catalysts containing 0.5 wt% Rh, 1 wt% Rh and 1:1 wt% RhPt supported on γ-alumina. Fresh and aged powder samples of the catalysts were characterized by $N_2$-BET, $H_2$ chemisorption, XRD, $H_2$-TPR, $O_2$-TPO and TEM analyses. The aim of this study is to bridge the gap of knowledge concerning the role of the preparation technique of Rh-based monolithic catalyst for use in diesel reforming.

## 2. Experimental

### 2.1. Catalyst preparation

Incipient wetness and reverse microemulsion techniques were used for catalyst preparation. The metal precursors used for the preparation of the IW catalyst were Rh nitrate ($Rh(NO_3)_3$, Rh 8–10%, w/w, Sigma–Aldrich) and Pt nitrate ($(NH_3)_4Pt(NO_3)_2$, Pt 3–4%, w/w, Alfa Aesar) solutions. The alumina powder (PURALOX HP-14/150, Sasol Germany GmbH) was impregnated with the metals in accordance with the nominal weight loadings presented in Table 1. The metal solution was dripped onto the alumina and carefully mixed. This procedure was repeated twice, with a drying step at 110 °C for 3 h in between. The resulting powders were then calcined in air at 800 °C for 3 h.

The microemulsion samples were prepared, under continuous stirring, by mixing two different reverse micelle solutions; one solution containing the precipitating agent ammonia (99.99%, Alfa Aesar) and one containing the metal precursors Rh nitrate ($Rh(NO_3)_3$, Rh 8–10%, w/w, Sigma–Aldrich), Pt nitrate ($(NH_3)_4Pt(NO_3)_2$, Pt 3–4%, w/w, Alfa Aesar) and Al nitrate ($Al(NO_3)_3{\cdot}9H_2O$, 99.99%, Alfa Aesar). Triton® X-100 (Alfa Aesar) was employed as surfactant, 1-hexanol (99%, Alfa Aesar) as co-surfactant and cyclohexane (99%, Alfa Aesar) as the oil phase. The volumetric ratio of the water/surfactant/co-surfactant/oil phase employed was (1.5/1.0/1.2/7.2). A similar volumetric ratio has been reported by Wang et al. [27]. In this study, the water solution, containing the nitrates and deionized water, was slowly added, drop by drop, onto the Triton® X-100, cyclohexane and 1-hexanol mixture. This procedure was carried out until the appearance of the latter was transformed from a milky viscous liquid into a transparent single phase mixture. Ammonia was then carefully added to the transparent mixture under stirring, at $T$ = 25 °C, until pH = 8.5 was reached. The resulting precipitate was stirred for 24 h, centrifuged for 1 h at 4000 rpm, decanted and washed with ethanol. The resulting powder was dried overnight at 80 °C. The powder material was then calcined in air using a heating ramp set to 0–200–500–800 °C to remove potential surfactants and other impurities. The calcination temperature was kept at the end of each interval (200, 500 and 800 °C) for 3 h, and the ramp speed was set to 5 °C/min.

After calcination, all IW and ME powders were suspended in ethanol slurry (~20 wt% powder), ball milled for 24 h and deposited via a dip-coating procedure on 400 cpsi cordierite monoliths, $d$ = 20.5 mm, $l$ = 30.5 mm (Corning). The dip-coating procedure was repeated until catalyst loadings of 20 wt% of the total weight (monolith and catalyst material) were reached. The coated monoliths were then calcined in air at 800 °C for 3 h. Table 1 exhibits the washcoat properties of the IW and ME monolithic catalyst used in this study.

### 2.2. Characterization

The catalyst powder samples in this study were characterized by the following techniques:

- Nitrogen adsorption at liquid $N_2$ temperature ($N_2$-BET) was used to measure the surface area, pore volume and pore size distribution of the fresh samples. A Micromeritics ASAP 2010 instrument

**Table 1**
Washcoat properties of fresh incipient wetness (IW) and microemulsion (ME) alumina-supported Rh and RhPt catalysts. The surface area and porosity were measured by $N_2$-BET, the dispersion and crystallite size of Rh were determined by $H_2$ chemisorption, while the crystallite size of Pt was determined by XRD.

| Catalyst[wt%] | Surface area[$m^2$/g] | Pore volume[$cm^3$/g] | Pore diameter[Å] | H/Rh[%] | $d_p$(Rh)[nm] | $d_p$(Pt)[nm] |
|---|---|---|---|---|---|---|
| $Rh_{0.5}$-IW | 131 | 0.93 | 285 | 58 | 1.9 | n.a. |
| $Rh_{1.0}$-IW | 134 | 0.95 | 282 | 56 | 2.0 | n.a. |
| $Rh_{1.0}Pt_{1.0}$-IW | 132 | 0.92 | 278 | n.a. | n.a. | 30[a] |
| $Rh_{0.5}$-ME | 285 | 1.24 | 192 | 66 | 1.7 | n.a. |
| $Rh_{1.0}$-ME | 268 | 1.23 | 183 | 60 | 1.8 | n.a. |
| $Rh_{1.0}Pt_{1.0}$-ME | 277 | 1.33 | 191 | n.a. | n.a. | 17[b] |

[a] Pt crystallite size was measured at $2\theta = 86^\circ$ using the Scherrer equation.
[b] Pt crystallite size was measured at $2\theta = 40^\circ$ using the Scherrer equation.

was employed. Prior to the analysis the sample, ~0.4 g, was degassed in vacuum for 3 h at 250 °C.

- X-ray diffraction (XRD) was used to determine the crystal phases of the fresh samples. A Siemens Diffraktometer D5000 scanning $2\theta$ from 10° to 90° in the scan mode (0.02°, 1 s), using Ni filtered Cu Kα radiation was employed.
- Temperature programmed reduction (TPR) was performed to determine the reducibility of the fresh samples. Approximately 0.1 g sample was reduced in hydrogen, 5 vol.% $H_2$ in Ar (50 $cm^3$/min), in the temperature range of 30–1000 °C with the heating rate set to 10°/min. A Micromeritics Autochem 2910 equipped with a thermal conductivity detector (TCD) was employed. Temperature-programmed oxidation (TPO) was performed to distinguish the type and amount of coke that was present on the aged samples. Approximately 0.1 g of aged sample was collected and heated in oxygen, 5 vol.% $O_2$ in Ar (50 $cm^3$/min), in the temperature range of 30–1000 °C with the ramp speed set to 10 °C/min. The same instrument as mentioned previously was employed.
- Hydrogen chemisorption analysis was used to measure the dispersion and the crystallite size of the Rh particles in the monometallic fresh samples by using a Micromeritics ASAP 2020. The sample, ~0.2 g, was pre-reduced by hydrogen at a temperature set to 950 °C, helium treated at 450 °C and finally hydrogen treated and analyzed at 40 °C. The atomic stoichiometric value of H/Rh = 1 was used for processing of the chemisorption data.
- Transmission electron microscopy (TEM) was used to determine the composition, morphology and particle size distribution of Rh and Pt species of the fresh and aged $Rh_{1.0}Pt_{1.0}$-IW and $Rh_{1.0}Pt_{1.0}$-ME samples. The samples were collected and transferred onto a carbon film containing holes supported by a 200 mesh TEM grid of copper. The powders, ~0.1 g/sample, were gently ground using a pestle and mixed in a solvent containing ~2–3 droplets of n-buthanol. A droplet of the solution was then added to the TEM grid and dried. A JEM 2000FXII (JEOL) was used to image the particles size distribution (≥10 nm) on the alumina support. Images with high resolution were recorded using a transmission electron microscope equipped with a field emission gun, JEM 2100F (JEOL), and an energy dispersive X-ray (EDX) spectrometer, JED 2300 (JEOL).

In this study, fresh powder samples were analyzed by $N_2$-BET, XRD, $H_2$ chemisorption, $H_2$-TPR, and TEM analyses. The fresh powder samples were taken from the catalyst preparation prior to deposition on the monoliths. Aged powder samples were analyzed by $O_2$-TPO and TEM analyses. The aged powder samples were taken from the washcoats of the aged monoliths, which were assembled after the ATR experiments were completed. The samples were collected by cutting the aged monoliths in half and scraping off the interior washcoat by using a scalpel knife.

### 2.3. Low-sulfur diesel reforming

The diesel reforming experiments were carried out at a reaction condition of $T_{feed}$ = 650 °C, $H_2O/C \sim 2.5$, $O_2/C \sim 0.49$, TOS = 3 h, GHSV ~ 13 000 $h^{-1}$ and $P$ = 1 atm. A standard diesel fuel (S ~ 6 ppm, C/H ~ 6.43(w/w)) whose physical and chemical properties are in close correlation to Swedish Environmental Class 1 diesel (MK 1), was used as feedstock [28]. The experiments were carried out in a vertically mounted stainless steel tubular reactor with ID = 23.7 mm equipped with a heating coil and three thermocouples to control the feed and reactor temperatures. The product gases were analyzed using a Gasmet Cr-200 Fourier Transform Infrared Spectrometer (FTIR) and a Maihak modular system S710 equipped with a non-dispersive infrared sensor (NDIR) and TCD. Further details concerning the fuel properties, reactor set-up and experimental procedure can be found in previous studies [16,17].

## 3. Results and discussion

### 3.1. Catalyst characterization

#### 3.1.1. BET

The textural data of the fresh IW and ME powder samples obtained from the $N_2$ sorption measurements are presented in Table 1. As seen in the table, the highest surface areas are noted for the ME prepared samples. Furthermore, an increase of the Rh metal loading on the alumina support had a slightly negative effect on the surface area. The addition of the Pt addition had the opposite effect. The BET surface areas for $Rh_{0.5}$-ME, $Rh_{1.0}$-ME and $Rh_{1.0}Pt_{1.0}$-ME were 285, 268 and 277 $m^2$/g, respectively. The high surface areas may be ascribed to smaller particle size and better dispersion of the synthesized active metal particles on the support. These attributes are characteristic for ME prepared samples [22–26]. These particle sizes and metal–support interaction trends can be found in the results obtained from the $H_2$ chemisorption, $H_2$-TPR and TEM analyses. These results will be discussed in details in Sections 3.1.2, 3.1.4 and 3.1.6, respectively.

For the IW catalyst, the impregnation of the active metals on the support and the high calcination temperature employed at 800 °C resulted in a small decrease of BET surface areas. The γ-$Al_2O_3$ powder used in the synthesized IW catalysts had an initial surface area of 150 $m^2$/g. The BET surface areas for $Rh_{0.5}$-IW, $Rh_{1.0}$-IW and $Rh_{1.0}Pt_{1.0}$-IW were 131, 134 and 132 $m^2$/g, respectively.

#### 3.1.2. $H_2$ chemisorption

The results from the $H_2$ chemisorption measurements of the fresh monometallic IW and ME samples are also presented in Table 1. As seen in the table, the highest rhodium dispersions are noted for the ME samples. For $Rh_{0.5}$-ME the H/Rh was ~66%, ~10% higher than for the IW sample with corresponding Rh loading. For $Rh_{1.0}$-ME, the double metal loading of rhodium on the

alumina support decreased the dispersion to ~60%. This reduction is expected as an increased loading of rhodium within the alumina pores with defined spaces, increases the probability of agglomeration of the noble metal particles taking place both during the synthesis and calcination stages. For the IW sample $Rh_{0.5}$-IW, high rhodium dispersion was noted, ~58%, with an average Rh crystallite size ~1.9 nm. For $Rh_{1.0}$-IW, a slightly lower dispersion, ~56%, and larger average Rh crystallite size ~2.0 nm were measured.

The chemisorption results of the ME samples follow the same trends as reported by others, lower crystallite and particle sizes are typically reported for ME prepared samples [22–26]. In general, a particle can be defined as an agglomeration of several crystallites. Therefore, in order to validate the characterization results, the particle size should exceed the size of a crystallite. In this work, $H_2$ chemisorption and XRD analyses (see Section 3.1.3) were used to determine the crystallite size of Rh and Pt (Table 1). TEM analysis was used to measure the particle size of Rh and Pt (see Section 3.1.5).

As seen in Table 1, the average Rh crystallite size for the ME samples ranges from 1.7 to 1.8 nm. Other groups have reported very small Rh particles with size diameter in the interval of 1.5-5.0 nm for ME prepared samples [29–32]. For instance, the size control of Rh on $SiO_2$ by ME preparation was investigated by Hanaoka et al. [31] where they found that the Rh particle size to be dependent on the length of the HC in the alcohol used as the co-surfactant and the chemical nature of the surfactant. The smallest Rh particle ~1.5 nm in average size was managed by using 1-butanol and polyoxyethylene oleyether. Also, a study by Kishida et al. [32] showed that the Rh particle size, ~1.5–2 nm, on $SiO_2$ was favored by lower synthesis temperature in the interval of 0–25 °C. However, it should be noted that the ME recipes employed by the Hanaoka and Kishida groups involved using the ingredients chloride salts as Rh precursor and hydrazine as reducing agent. Chlorides are stable compounds difficult to remove e.g. during the calcination stage [33] and thus can be present on alumina e.g. during reforming of diesel. Hydrazine is a very reactive reducing agent that needs to be handled with care both during the catalyst preparation as well as during the recovery of the solvent in the liquid phase after the final stage of the ME synthesis is completed [22,23].

Scarce information can be found in the literature regarding crystallite and particle size of bimetallic Rh–Pt catalysts prepared by ME. Typically reported noble-metal bimetallic ME samples are Ru–Pt formulations used as electrocatalysts for PEFC and direct methanol fuel cells (DMFC) [34–36]. In this study, $H_2$ chemisorption analysis was not performed for the bimetallic IW and ME samples since it is difficult to interpret from the results whether hydrogen adsorbs solely on rhodium or on platinum particles, or on Rh–Pt alloys. Instead a TEM analysis, described in detail in Section 3.1.6, was done to get a better overview of the different Rh and Pt particle size distributions and surface states on alumina.

### 3.1.3. X-ray diffraction

The crystalline bulk phases of the fresh samples $Rh_{1.0}Pt_{1.0}$-IW and $Rh_{1.0}Pt_{1.0}$-ME identified from the X-ray diffraction measurements are shown in Fig. 1. The XRD patterns showed that the γ-phase of alumina is present for both samples. Also, ME was found to be less crystalline. Zhang et al. [37] have presented similar ME alumina diffraction peaks. In this study, Rh phases were not detected by XRD indicating that the rhodium particles are small and well-dispersed on the support. This confirms the results from the $H_2$ chemisorption analysis where the Rh crystallite size for the IW and ME samples was in the range of 1.7–2.0 nm, as seen in Table 1. In Fig. 1, peaks ascribed to metallic Pt [38,39] were observed at $2\theta = 40$, 46.5, 81.5 and 86°. The crystallite size of Pt was ~30 nm for the IW sample and ~17 nm for the ME sample (Table 1). It is possible that the high calcination temperatures at 800 °C, employed during the catalyst preparation stage, may have caused formation and agglomeration of the metallic Pt particles. In general, platinum oxides, e.g. PtO and $PtO_2$, are unstable and can easily decompose and form metallic Pt at temperatures above 500 and 550 °C, respectively [40–42]. Also, Pt particles sinter at temperatures exceeding 450 °C [10]. Furthermore, recent TEM studies have shown that Pt particles migrate more easily on alumina than on other supports such as zirconia [43,44].

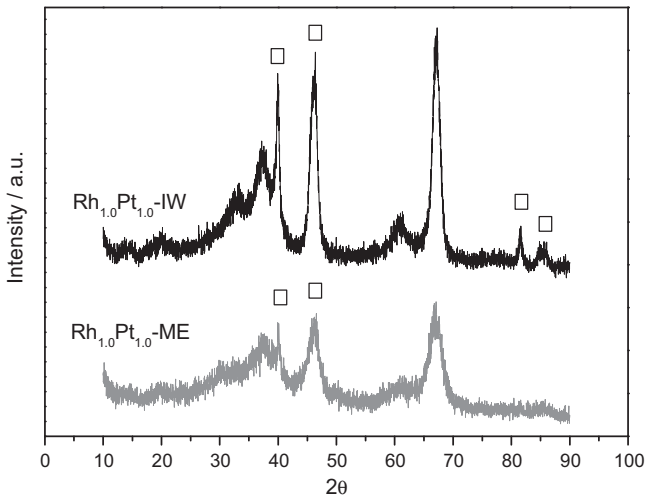


**Fig. 1.** XRD patterns for $2\theta$ between 10° and 90° at room temperature of $Rh_{1.0}Pt_{1.0}$-IW and $Rh_{1.0}Pt_{1.0}$-ME. Reflections of (□) metallic Pt. See Table 1 for catalyst formulation.

### 3.1.4. Temperature-programmed reduction

$H_2$-TPR profiles of fresh powder samples $Rh_{1.0}$-IW, $Rh_{1.0}Pt_{1.0}$-IW, $Rh_{1.0}$-ME and $Rh_{1.0}Pt_{1.0}$-ME are displayed in Fig. 2a and b. Overall four peaks can be identified; one small at 100 °C which may be ascribed to reduction of bulk rhodium oxides, one smaller at 200 °C denoted to possible strong rhodium interactions with the support, one major at 450 °C which is due to hydrogen spillover effect on the support and finally another major peak at 800 °C which may be ascribed to reduction of rhodium aluminates [33]. Based on this latter observation, the pre-reduction temperature during the $H_2$ chemisorption analysis was set at 950 °C in order to make sure that all rhodium species was reduced, even the rhodium aluminates present at 700–900 °C (Fig. 2a and b), prior to the helium treatment at 450 °C and the sequential chemisorption analysis performed at $T = 40$ °C (see Section 2.2). This in order to obtain an accurate reading and value of the Rh dispersion on the alumina supports.

As seen in Fig. 2a and b the TCD signals for the registered peaks ascribed to rhodium species were low indicating that the majority of the rhodium species were non-reducible and strongly bonded to the support. Similar observations have been reported in a previous study [16] and by others [33,45,46]. The strong rhodium–alumina interactions may have been caused by the high calcination temperature employed in this study, 800 °C. At this calcination temperature, rhodium particles become highly mobile and may enter defects and voids in the alumina support making them inaccessible for hydrogen reduction [45]. The effect of calcination temperature on 1 wt% $Rh/Al_2O_3$ was demonstrated by Burch et al. [46] where the resultant $H_2$-TPR profiles clearly showed significant losses of reducible rhodium species at calcination temperatures exceeding 500 °C.

In this study, two clear trends can be observed from the TPR profiles. First, the hydrogen uptake for the IW samples (Fig. 2a) was

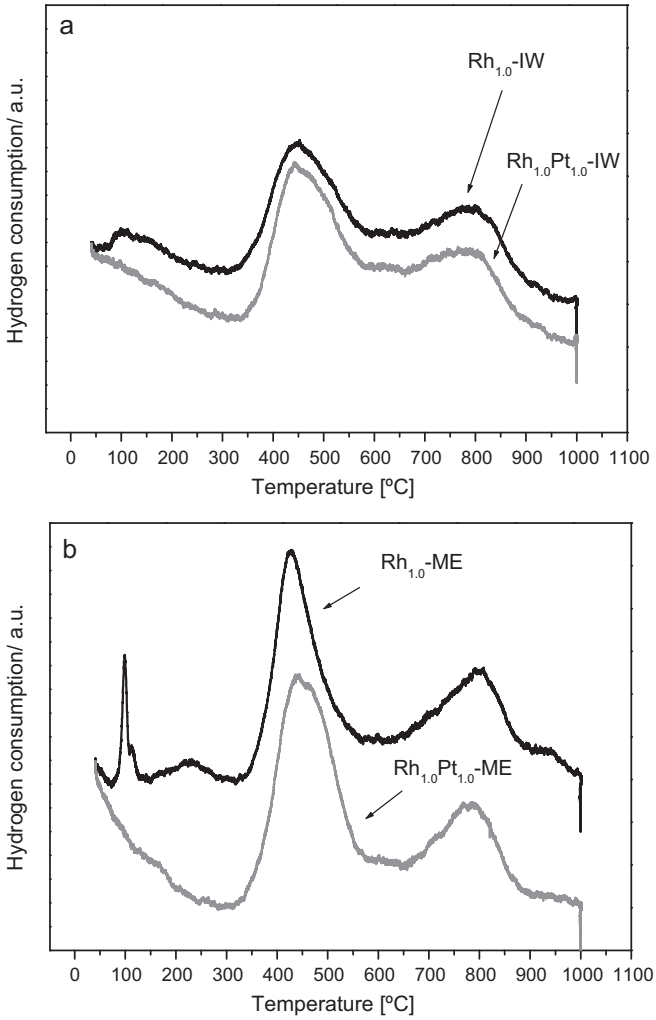


**Fig. 2.** TPR profiles of (a) $Rh_{1.0}$-IW and $Rh_{1.0}Pt_{1.0}$-IW and (b) $Rh_{1.0}$-ME and $Rh_{1.0}Pt_{1.0}$-ME. The hydrogen consumption is displayed as function of temperature. See Table 1 for catalyst formulation.

found to be lower than for the ME samples (Fig. 2b). For instance, the TPR profile for sample $Rh_{1.0}$-ME shows a much more distinctive and sharper peak at 100 °C and a peak also at 200 °C compared to $Rh_{1.0}$-IW. The lower reducibility of the IW samples may be due to the lower Rh dispersion of these samples, 56–58%, compared to the ME samples, 60–66%, as seen in Table 1.

Another trend that can be noted in the TPR profiles is that the addition of Pt onto the alumina support lowered the reducibility of the different rhodium species. This trend was notable both for the IW and ME bimetallic samples. The largest reduction was noted for the bulk rhodium oxides as no peaks were detected at 100 °C. The peaks at 400 and 800 °C ascribed to the reduction of support and rhodium aluminates were only slightly lowered. A possible explanation to this reduction trend is that Pt forms RhPt alloys with Rh leading to a decrease of accessible rhodium oxides and rhodium aluminates on the support. This alloy formation trend can also be seen on the TEM analysis, which is discussed in detail in Section 3.1.6. As for the Pt particles not present in any alloy formation, it is unlikely that these particles were reduced by hydrogen during $H_2$-TPR as e.g. the XRD analysis showed that the Pt content in the fresh IW and ME samples was metallic (Fig. 1). The TEM analysis, which is discussed in detail in Section 3.1.5, showed similar results of Pt state for this group of single Pt particles.

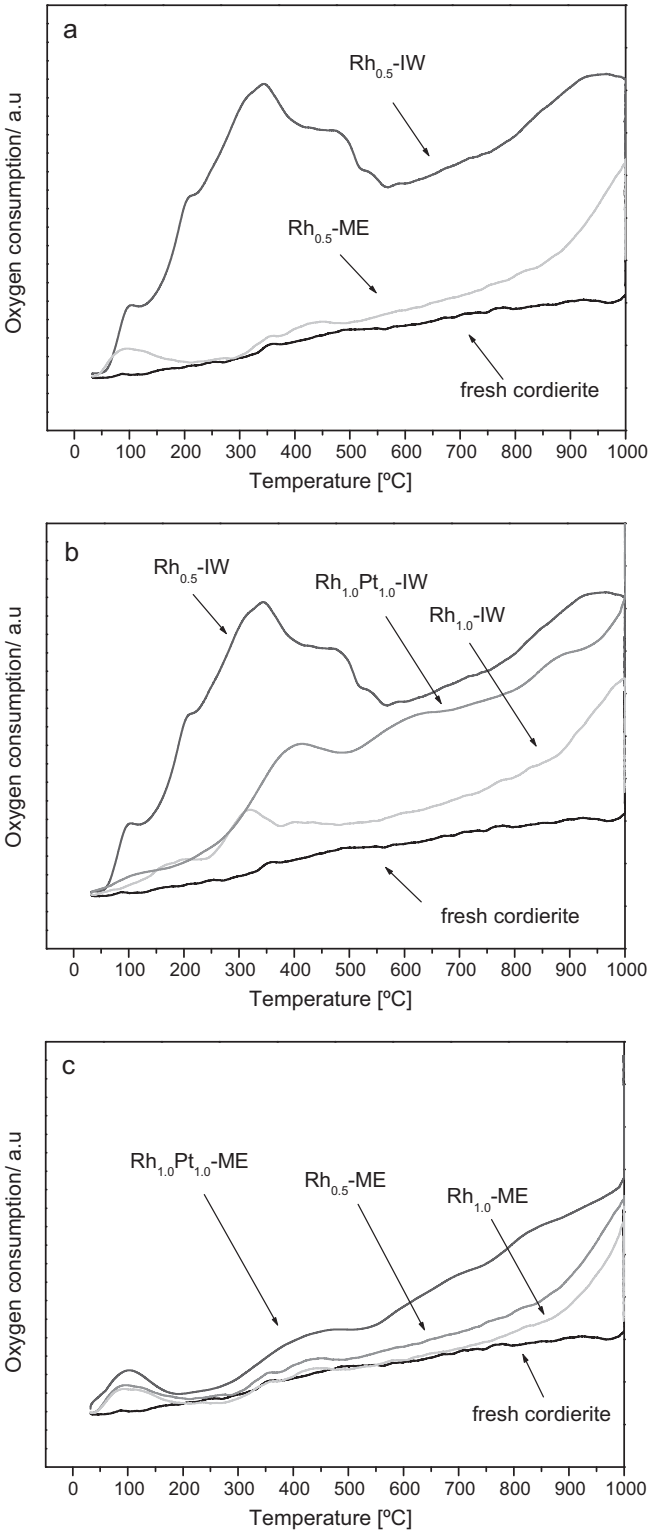


**Fig. 3.** TPO profiles of aged IW and ME catalysts, and fresh cordierite. The oxygen consumption is displayed as function of temperature. See Table 1 for catalyst formulation.

### 3.1.5. Temperature-programmed oxidation

TPO profiles of the aged IW and ME samples are presented in Fig. 3a–c. In Fig. 3a the TPO profiles of $Rh_{0.5}$-IW and $Rh_{0.5}$-ME are displayed. Typically, CO and $CO_2$ are formed and measured by TCD during the $O_2$-TPO treatment of the carbon deposited aged powder samples of the catalysts. The intensity of the TCD signals is

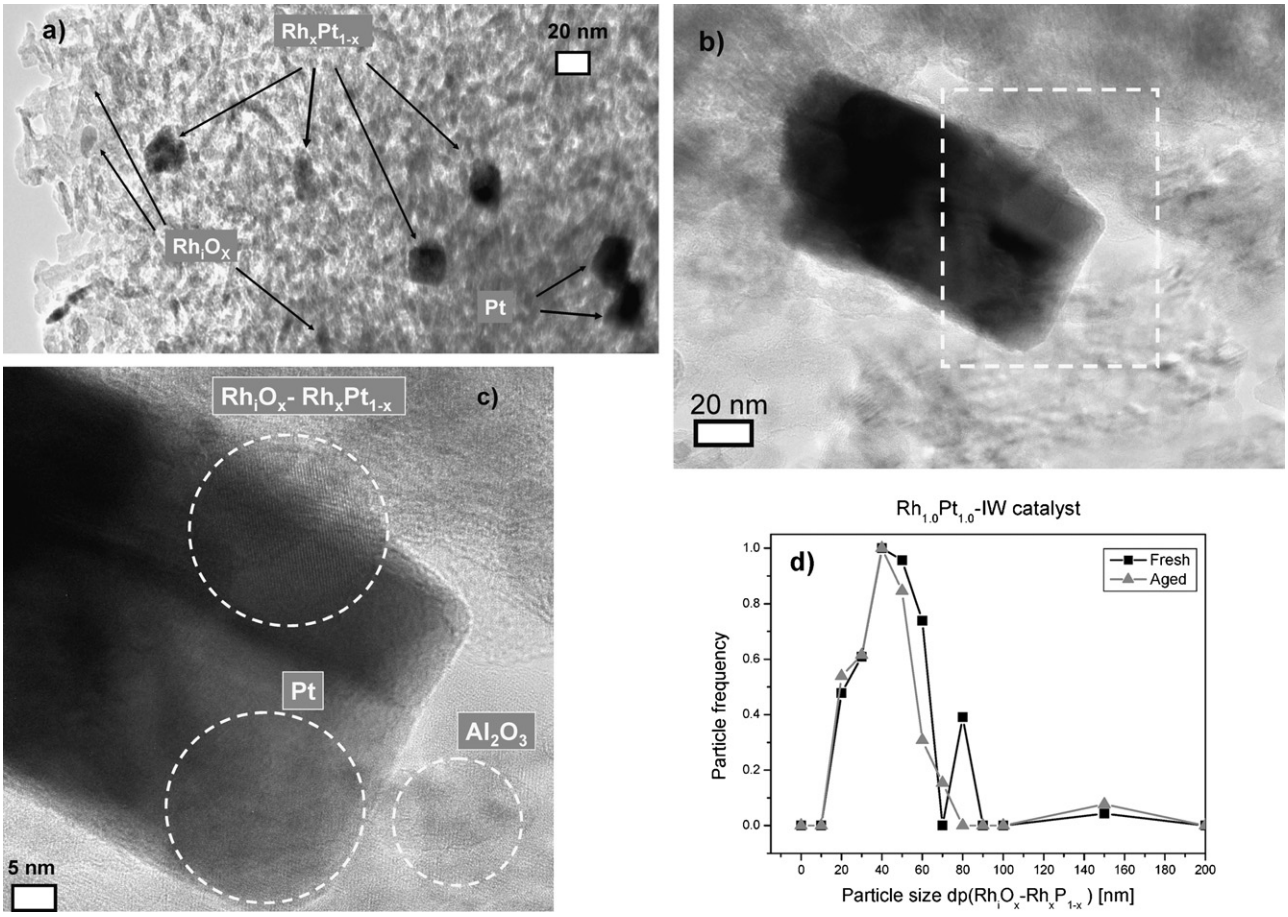


**Fig. 4.** (a–c) TEM images of typical $Rh_xPt_{1-x}$ alloy, rhodium oxides $Rh_iO_x$ and metallic Pt particles found in a fresh powder sample of $Rh_{1.0}Pt_{1.0}$-IW. The different phases were determined using EDX analysis. (c) An enlargement of (b), in which a possible $Rh_iO_x$–$Rh_xPt_{1-x}$ alloy crystal formation is displayed. (d) Particle size distributions of $Rh_iO_x$–$Rh_xPt_{1-x}$ alloys in the fresh and aged powder samples of $Rh_{1.0}Pt_{1.0}$-IW.

an indicator of the amount of coke present on the catalyst surface and bulk reacting with oxygen and forming CO and $CO_2$. As seen in the figures, overall four peaks were observed indicating that a variety of agglomerated carbonaceous species was present on the aged catalyst. The initial small oxidation peak detected at ~100 °C is ascribed to possible carbon formation on the surface active metals, the second peak in the interval ~300–400 °C may be due to coke deposits on bulk metallic centers, while the third peak in the interval ~500–600 °C may be due to coke species on the support [47,48]. Regarding the final peak at ~1000 °C, it may be ascribed to oxidation of unconverted graphite that is still present in the samples [49,50].

In this study, interestingly, e.g. as seen in Fig. 3a, an overall lower formation of coke was present on the ME samples. This latter attribute is beneficial as it may prolong the diesel reforming catalyst lifetime considerably, since a lower degree of carbon deposition results in less risk of blocking active sites and pores [51,52]. Other research groups have reported similar results regarding carbon-tolerant ME catalysts [25,53,54]. In these studies, it was suggested that the coke endurance ability was due to stronger metal–support interactions and smaller particle sizes. The latter feature was noted for nickel ME catalyst tested for methane reforming [54]. It was found that these catalysts had the smallest Ni particle size distributions, which leads to less extent of deposition of carbon whiskers on the periphery of the particles during reforming. This ME property may also explain the positive TPO trends noted in this study as the $H_2$ chemisorption showed that the Rh average crystallite size was smallest for the ME prepared samples, ~1.7–1.8 nm (Table 1).

In Fig. 3b, TPO profiles of the IW samples are presented. The most intense peaks are noted for sample $Rh_{0.5}$-IW, followed by $Rh_{1.0}Pt_{1.0}$-IW and $Rh_{1.0}$-IW. Hence, the increase of Rh metal loading lowered the formation of coke, while the addition of Pt on the alumina support had the opposite effect. Regarding the Rh trend, different results can be found in the literature were e.g. some groups report that an increased Rh loading has a positive effect on hindering adsorption of surface carbon species [55] while others suggest that the Rh loading has little effect [56]. Regarding the Pt-addition trend, similar negative TPO trends have been noted in a previous study by the present group [16] as well as by others [47,57].

In Fig. 3c, the TPO profiles of the ME samples are presented. The most intense peaks are noted for sample $Rh_{1.0}Pt_{1.0}$-ME, followed by $Rh_{0.5}$-ME and $Rh_{1.0}$-ME. Hence, again, the same TPO trends in terms of Rh metal loading and Pt addition are noted.

### 3.1.6. Transmission electron microscopy

The dispersion, morphology and particle size distribution of rhodium and platinum on alumina for samples $Rh_{1.0}Pt_{1.0}$-IW and $Rh_{1.0}Pt_{1.0}$-ME, both in the fresh and aged states, are presented in Figs. 4a–d and 5a and b, respectively.

The TEM investigation of the fresh IW and ME powder samples containing 1 wt% Rh and 1 wt% Pt shows that the catalyst material is more homogeneously distributed over the washcoat material in the IW sample. In the TEM analysis, two particle number frequency maxima were noted for all measured particles, 20–50 nm and 80 nm for ME, and 30–60 nm and 80 nm for IW, respectively. The average diameter of the smallest single Rh-particles detected by TEM was approximately 10 nm for the ME sample, and 15 nm for the IW sample, respectively. For Pt, the smallest single particles detected were ~20 nm in diameter for the ME sample, and ~22 nm

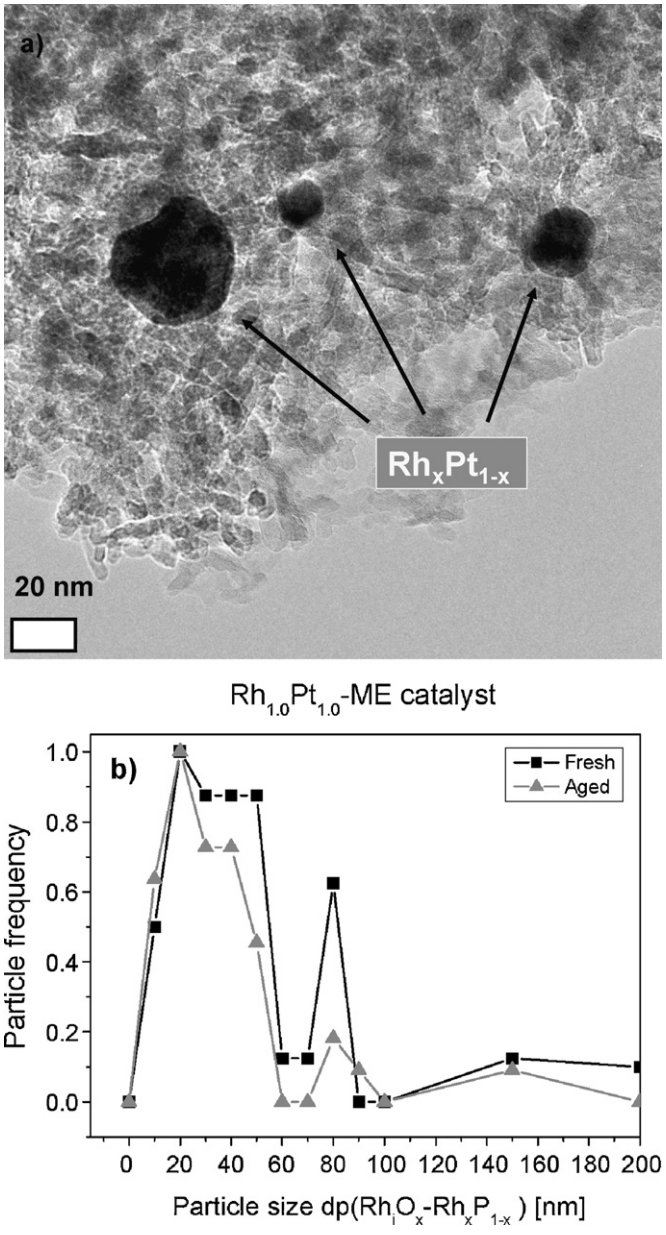


**Fig. 5.** (a) TEM images of typical $Rh_xPt_{1-x}$ alloy particles in a fresh powder sample of $Rh_{1.0}Pt_{1.0}$-ME. (b) Particle size distributions of $Rh_iO_x$–$Rh_xPt_{1-x}$ alloys in the fresh and aged powder samples of $Rh_{1.0}Pt_{1.0}$-ME.

for the IW sample, respectively. Hence, in general, smaller particle sizes of active metals were observed on alumina for the ME prepared samples. The differences in average sizes of the individual Rh and Pt particles between the IW and ME sample, measured by TEM, confirms the results from the $H_2$ chemisorption and XRD analyses as similar trends in crystallite sizes were noted, which can be seen in Table 1. Elemental analyses of the $Rh_{1.0}Pt_{1.0}$-IW and $Rh_{1.0}Pt_{1.0}$-ME powder samples reveal that some of the catalyst particles contain either Rh or Pt, but most of them have a composition indicating an alloy between them, $Rh_xPt_{1-x}$. These alloyed types of particles were observed for both the IW and ME materials, as seen in Figs. 4a and 5a, respectively. After calcination, carried out under oxidative conditions (in air), Rh will appear as $Rh_iO_x$ and Pt as metal while the alloys form a particle with Pt metal in contact with a crystal of $Rh_iO_x$ forming $Rh_xPt_{1-x}$ (see Figs. 4a and 5a). Hence, the presence of $Rh_iO_x$, metallic Pt and $Rh_xPt_{1-x}$ alloys confirms the results from the XRD and $H_2$-TPR analyses as seen in

**Table 2**
Activity results of the incipient wetness (IW) and microemulsion (ME) alumina supported Rh catalyst. The reaction condition for ATR of diesel was $T_{feed}$ = 650 °C, $H_2O/C \sim 2.5$, $O_2/C \sim 0.49$, TOS = 3 h, GHSV ~ 13 000 $h^{-1}$ and $P$ = 1 atm. See Table 1 for catalyst formulation.

| Catalyst | $X_{diesel}$[%] | $S_{CO_2}$[%] | $H_2$[vol.%] | $C_2H_4$[vol.%] |
|---|---|---|---|---|
| $Rh_{0.5}$-IW | 96.1 | 51 | 26 | 0.31 |
| $Rh_{1.0}$-IW | 95.8 | 54 | 22 | 0.28 |
| $Rh_{1.0}Pt_{1.0}$-IW | 94.5 | 57 | 24 | 0.44 |
| $Rh_{0.5}$-ME | 92.8 | 55 | 22 | 0.24 |
| $Rh_{1.0}$-ME | 95.6 | 52 | 27 | 0.27 |
| $Rh_{1.0}Pt_{1.0}$-ME | 95.1 | 52 | 25 | 0.34 |

Figs. 1 and 2a and b, respectively. Regarding $Rh_iO_x$ species, typically $Rh_2O_3$ is found at this temperature as it is are known to be stable up to 1000 °C [58]. It is also possible that $Rh_2O_3$ can form bonds directly with $Rh_xPt_{1-x}$ alloys. A possible crystal formation of a $Rh_iO_x$–$Rh_xPt_{1-x}$ bond can be seen in Fig. 4b and c. Kaila et al. [15] and Okumura et al. [59] have made similar observations. As seen in the particle size distribution plots in Figs. 4d and 5b, the particle number frequency maximum for $Rh_iO_x$–$Rh_xPt_{1-x}$ alloys, in the fresh state, was 20 nm for the ME sample and 40 nm for the IW sample, respectively. Hence, as seen in Figs. 4d and 5b, smaller particles and slightly narrower particle size distributions, e.g. in the interval of 0–60 nm, were noted for the ME prepared samples. In this study, it was difficult to determine from the TEM images the geometry and orientation of the individual Rh and Pt crystals. Most of the Rh species appeared rounded while different shapes and sub layers of crystals where detected for the Pt particles. Other groups have reported that Rh, present in oxidative environment e.g. in the form of $Rh_2O_3$, has a typical orthorhombic structure at $T \sim 500$–900 °C [58]. Regarding the orientation, typically (1 1 1) and (1 1 0) are reported for Rh and Pt crystals, respectively, formed at $T > 500$ °C [45,60,61].

For the aged IW and ME powder samples, no significant sintering effects and carbon deposits were noted. An interesting TEM image observation was that most of the $Rh_iO_x$ crystals, both found separately and with an $Rh_xPt_{1-x}$ alloy, were found to shrink in size. A possible explanation to the shrinking phenomenon is that $Rh_iO_x$ species switch oxidation state from e.g. $Rh^{3+}$ to metallic $Rh^0$. A similar observation was noted in a previous study where a reducing environment was found predominant during ATR of diesel causing the formation of metallic $Rh^0$ [16]. This phenomenon can also be seen in this study in the alloy particle size distribution plots in Figs. 4d and 5b by comparing the fresh samples (black line) with the aged samples (gray line). The particle number frequency maximum for the aged $Rh_iO_x$–$Rh_xPt_{1-x}$ alloy noted at e.g. 80 nm, dropped from 0.4 to almost zero for the IW sample, and from 0.6 to 0.2 for the ME sample, respectively. These significant drops may be explained by a possible particle shrinkage phenomenon occurring, caused by a reduction of the oxide group in the molecular structure of the $Rh_iO_x$ crystals, and as a result the overall particle size for the $Rh_iO_x$–$Rh_xPt_{1-x}$ alloy is reduced. No phase transition was detected for any Pt species as they all remained in the metallic state. These phenomena were noted for both the aged IW and ME samples. Similar observations of Rh phase transition and Pt state in aged diesel reforming catalyst were noticed in a previous study using XPS analysis [16].

### 3.2. Catalyst activity

The catalytic performance of the IW and ME samples at ATR reaction condition $H_2O/C \sim 2.5$ and $O_2/C \sim 0.49$ are presented in Table 2. The activity measurements include the diesel conversion, the $CO_2$ selectivity parameter (expressed as $CO_2/(CO_2 + CO)$), as well as the hydrogen and ethylene concentrations in the reformate. Details

concerning the calculations of the diesel conversion can be found in a previous study [16].

*3.2.1. IW catalyst*

The reforming activity for the $Rh_{0.5}$-IW catalyst was high as the diesel conversion was measured to be 96.1%. The $CO_2$ selectivity was also high, approximately 51%. The hydrogen concentration in the product gas was 26 vol.% while the ethylene concentration was much lower ~0.31 vol.%. For the $Rh_{1.0}$-IW similar activity results, e.g. in terms of diesel conversion, were noted. For the bimetallic sample $Rh_{1.0}Pt_{1.0}$-IW the diesel conversion was slightly lower. Furthermore, the ethylene concentration was the highest out of all samples, close to 0.45 vol.%.

*3.2.2. ME catalyst*

The activity results in Table 2 show that the ME prepared catalysts are highly active and capable of catalytically reforming the molecules in the diesel fuel to obtain high fuel conversion. As seen in Table 2, the reforming activity for the $Rh_{0.5}$-ME was high as the diesel conversion was measured to be 92.8%. The $CO_2$ selectivity was also high, approximately 55%. The hydrogen concentration was 22 vol.% while the ethylene concentration was significantly lower ~0.24 vol.%. For the $Rh_{1.0}$-ME higher activity results were noted e.g. in terms of diesel conversion. For the bimetallic sample $Rh_{1.0}Pt_{1.0}$-ME the activity results were lower than for the $Rh_{1.0}$-ME. Also the ethylene concentration in the reformate was the highest, ~0.34 vol.%.

*3.3. Final remarks: possible trends and correlations between the activity and characterization data*

The activity results presented in Table 2 established that low weight loadings of rhodium and rhodium–platinum formulations on alumina are highly active for ATR of diesel, as fuel conversions above 92% were obtained. These results are in line with what has been reported in the literature by our group and by others [15,16]. In this study, high diesel conversions were achieved regardless of employed catalyst preparation technique. This feature is positive as a good fuel economy is crucial for diesel trucks, in particular for possible FC-APU utilities. For instance, high fuel slip from the reformer can deactivate the fuel cell in a PEFC-APU based system. The long hydrocarbon chains in diesel can easily become caught in the pores of the Nafion membranes, hindering the transport of the hydrogen ions from the anode to the cathode side [10,62]. In this study the high $CO_2$ selectivity noted for both the IW and ME samples, ~51–57%, is also positive as high CO concentrations are known to deactivate PEFC due to CO adsorption on the normally Pt-coated anode electrodes. Typical examples are Pt/C and PtRu/C formulations [10,62].

In this study, some general trends can be noted in the activity data in Table 2. It can be seen that the diesel conversion is closely coupled to the $CO_2$ selectivity and hydrogen production. An increased diesel conversion typically results in a decrease in the $CO_2$ selectivity and a higher hydrogen production (in all cases expect for the $Rh_{1.0}$-IW catalyst). For instance, the highest diesel conversion, 96.1 and 95.8%, and hydrogen generation, 26 and 27 vol.%, were noted for samples $Rh_{0.5}$-IW and $Rh_{1.0}$-ME, respectively.

Another trend that can be seen in the activity data in Table 2 is that the addition of Pt resulted in an overall lower catalyst activity. This reduction trend was noted for the IW and ME bimetallic samples. The addition of platinum to the washcoat decreased the diesel conversion from 95.8 to 94.5% for $Rh_{1.0}Pt_{1.0}$-IW and 95.6 to 95.1% for $Rh_{1.0}Pt_{1.0}$-ME, respectively. This reduction in reforming activity may be explained by the TPR profiles. As seen on Fig. 2a and b the addition of Pt was found to eliminate accessible bulk rhodium oxides and also decrease reducible rhodium aluminates on the supports. Also, TEM analysis showed that $Rh_xPt_{1-x}$ alloys were found predominantly on the alumina support, regardless of employed preparation technique (see Figs. 4a and 5a). Furthermore, most of the single Rh particles were found in the oxidized state, e.g. as $Rh_2O_3$, while the Pt particles were found in the metallic state. Regarding the Rh state, results from previous work from our group [16] showed that the degree of available rhodium oxide species on alumina was favorable for ATR of diesel. It was found that the diesel conversion was strongly correlated to the amount of accessible bulk and surface $Rh_iO_x$ on the alumina support. Other groups have reported similar results regarding the importance of generating active metal sites in the form of rhodium oxide species [55,63,64]. Hence, in this study, the lower development of rhodium oxide species in the bimetallic IW and ME samples may very well explain the overall lower reforming activity. Regarding the Pt state, limited studies can be found in the literature where the role of surface and bulk states of Pt has been investigated for ATR of diesel. Studies by Kaila et al. [15] have reported the presence of metallic Pt in $Pt/ZrO_2$ and $RhPt/ZrO_2$ diesel reforming catalysts calcined at ~900 °C. In their study it was noted that the $Pt/ZrO_2$ catalyst had the lowest activity as it was deactivated by extensive carbon deposition and particle sintering of the metallic Pt particles [15]. The addition of Rh improved the catalyst activity e.g. by inhibiting Pt migration and sintering on the support.

Finally, in this study, the measured ethylene concentrations can to some extent be correlated with the $O_2$-TPO data. In ATR of diesel ethylene is a known coke precursor. High ethylene concentrations are often an indication of severe carbon deposition taking place on the reforming catalyst [51,52]. This is detrimental as it often leads to significant reduction of the diesel reforming catalyst's long term performance as the active surface sites of the catalyst are blocked by various types of carbon deposits. In this study, the activity results showed that the overall highest ethylene concentrations were detected in the reformate from the IW samples, ~0.28–0.44 vol.% (Table 2). Also, the $O_2$-TPO measurements showed that higher loads of carbon deposits were detected for the IW samples, both on the active metals at $T \sim 100$ °C and on the support at $T \sim 600$ °C (Fig. 3b). Hence, IW prepared samples may have lower tolerance towards carbon deposition compared to ME prepared samples. This observation is in good agreement with what has been reported by others [25,53,54].

## 4. Conclusions

The results presented in this study provide a deeper understanding regarding possible reaction mechanisms occurring during ATR of diesel that can be correlated with the catalyst preparation and composition. IW and ME prepared catalysts with the composition 0.5 wt% $Rh/\gamma\text{-}Al_2O_3$, 1.0 wt% $Rh/\gamma\text{-}Al_2O_3$ and 1:1 wt% $RhPt/\gamma\text{-}Al_2O_3$ were tested in a bench-scale reactor at reaction conditions $T_{feed} = 650$ °C, $H_2O/C \sim 2.5$, $O_2/C \sim 0.49$, TOS = 3 h, GHSV ~ 13 000 $h^{-1}$ and $P = 1$ atm. All results were reproducible and steady-state conditions were established for all experiments. Fresh and aged powder samples of the washcoated cordierite monolithic catalyst were characterized using $N_2$-BET, XRD, $H_2$ chemisorption, $H_2$-TPR, $O_2$-TPO and TEM analyses.

The activity measurements showed that the IW and ME samples were comparable in terms of diesel conversion and hydrogen generation. The bimetallic samples generated more ethylene, which is an indication of carbon deposition taking place on the catalyst surface. This deactivation phenomenon was confirmed by $O_2$-TPO analysis of the aged samples where the measurements showed that the addition of Pt on the alumina resulted in higher loads of coke both on the active metals and on the support. Interestingly, these effects were less prominent on the ME prepared samples.

The other characterization measurements showed differences in morphology between the IW and ME samples. The largest differences where noted in terms of surface area and rhodium dispersion. The other characterization results were comparable, e.g. the γ-phase of alumina was detected by XRD and strong interaction of rhodium oxides with alumina with low reducibility towards hydrogen were registered during TPR measurements. The TEM analysis showed that mainly $Rh_xPt_{1-x}$ alloys with an average particle size of ~20–50 nm were present on the alumina support for the IW and ME bimetallic samples; both in the fresh and the aged states. For the aged samples, rhodium was found to switch oxidation state e.g. from $Rh^{3+}$ to $Rh^0$ while Pt remained in the metallic state.

## Acknowledgements

The Foundation for Strategic Environmental Research (MISTRA) is gratefully acknowledged for financial support. The Wallenberg Foundation is also acknowledged for financial support in the new electron microscopy facilities at MMK, SU. Thanks also to Corning Inc. for supplying cordierite substrates and to Sasol Germany GmbH for providing the alumina.

## References

[1] EPA, Anti Idling Regulations, www.epa.gov (accessed 22.09.10).
[2] Dieselnet, www.dieselnet.com (accessed 22.09.10).
[3] N. Lutsey, C.J. Brodrick, T. Lipman, Energy 32 (2007) 2428–2438.
[4] C.J. Brodrick, T.E. Lipman, M. Farshchi, N.P. Lutsey, H.A. Dwyer, D. Sperling, S.W. Gouse, D.B. Harris, F.G. King, Transp. Res. Part D 7 (2002) 303–315.
[5] F. Stodolsky, L. Gaines, A. Vyas, Analysis of Technology Options to Reduce the Fuel Consumption of Idling Trucks, ANL/ESD-43, Argonne National Laboratory, Argonne, 2000.
[6] M. Nilsson, Hydrogen generation for fuel cells in auxiliary power systems, PhD Thesis. KTH, Department of Chemical Engineering and Technology, TRITA-CHE Report 2009:7, ISBN:978-91-7415-245-6, 2009.
[7] B. Lindström, J.A.J. Karlsson, P. Ekdunge, L. De Verdier, B. Häggendal, J. Dawody, M. Nilsson, L.J. Pettersson, Int. J. Hydrogen Energy 34 (2009) 3367–3381.
[8] S. Specchia, A. Cutillo, G. Saracco, V. Specchia, Ind. Eng. Chem. Res. 45 (2006) 5298–5307.
[9] F. Barrato, U.M. Diwekar, J. Power Sources 139 (2005) 188–196.
[10] G. Kolb, Fuel Processing, Wiley-VCH Verlag GmbH & Co. KGaA, Weinheim, 2008.
[11] X. Karatzas, M. Nilsson, J. Dawody, B. Lindström, L.J. Pettersson, Chem. Eng. J. 156 (2010) 366–379.
[12] R.M. Heck, R.J. Farrauto, S.T. Gulati, Catalytic Air Pollution Control, 3rd ed., John Wiley & Sons, Inc., New York, 2009.
[13] X. Chen, A.R. Tadd, J.W. Schwank, J. Catal. 251 (2007) 374–387.
[14] P.M. Torniainen, X. Chu, L.D. Schmidt, J. Catal. 146 (1994) 1–10.
[15] R.K. Kaila, A. Gutiérrez, R. Slioor, M. Kemell, M. Leskelä, A.O.I. Krause, Appl. Catal. B 84 (2008) 223–232.
[16] X. Karatzas, J. Dawody, A. Grant, E.E. Svensson, L.J. Pettersson, Appl. Catal. B 101 (2011) 226–238.
[17] X. Karatzas, D. Creaser, A. Grant, J. Dawody, L.J. Pettersson, Catal. Today, doi:10.1016/j.cattod.2010.10.019.
[18] A.C. McCoy, M.J. Duran, A.M. Azad, S. Chattopadhyay, M.A. Abraham, Energy Fuels 21 (2007) 3513–3519.
[19] M. Nilsson, X. Karatzas, B. Lindström, L.J. Pettersson, Chem. Eng. J. 142 (2008) 309–317.
[20] D.J. Haynes, D.A. Berry, D. Shekhawat, J.J. Spivey, Catal. Today 136 (2008) 206–213.
[21] M. Harada, K. Takanabe, J. Kubota, K. Domen, T. Goto, K. Akiyama, Y. Inoue, Appl. Catal. A 371 (2009) 173–178.
[22] S. Eriksson, U. Nylén, S. Rojas, M. Boutonnet, Appl. Catal. A 265 (2004) 207–219.
[23] E. Elm Svensson, Nanotemplated high-temperature materials for catalytic combustion, PhD Thesis. KTH, Department of Chemical Engineering and Technology, TRITA-CHE Report 2008:46, ISBN:978-91-7415-019-3, 2008.
[24] S. Nassos, Development of catalytic nanomaterials for three industrial processes, PhD Thesis. Chalmers, Department of Chemical and Biological Engineering, ISBN 978-91-7291-949-5, 2007.
[25] M. García-Diéguez, I.S. Pieta, M.C. Herrera, M.A. Larrubia, L.J. Alemany, Appl. Catal. A 377 (2010) 191–199.
[26] R. Lanza, E. Eriksson, L.J. Pettersson, Catal. Today 147 (2009) S279–S284.
[27] X. Wang, G. Lu, Y. Guo, Y. Wang, W. Guo, Mater. Chem. Phys. 90 (2005) 225–229.
[28] The Swedish Petroleum Institute, SPI, www.spi.se (accessed 22.09.10).
[29] M. Ojeda, S. Rojas, M. Boutonnet, F.J. Pérez-Alonso, F.J. García-García, J.L.G. Fierro, Appl. Catal. A 274 (2004) 33–41.
[30] J.D. Hoefelmeyer, H. Liu, G.A. Somorjai, T.D. Tilley, J. Colloid Interface Sci. 309 (2007) 86–93.
[31] T. Hanaoka, T. Hatsuta, T. Tago, M. Kiskida, K. Wakabayashi, Appl. Catal. A 190 (2000) 291–296.
[32] K. Kishida, T. Hanaoka, W.Y. Kim, H. Nagata, K. Wakabayashi, Appl. Surf. Sci. 121/122 (1997) 347–350.
[33] C. Hwang, C. Yeh, Q. Zhu, Catal. Today 51 (1999) 93–101.
[34] S. Rojas, F.J. García-García, S. Järås, M.V. Martínez-Huerta, J.L.G. Fierro, M. Boutonnet, Appl. Catal. A 285 (2005) 24–35.
[35] T. Kim, K. Kobayashi, M. Nagai, J. Oleo Sci. 56 (2007) 553–562.
[36] L. Xiong, A. Manthiram, Solid State Ionics 176 (2005) 385–392.
[37] X. Zhang, F. Zhang, K. Chan, Mater. Lett. 58 (2004) 2872–2877.
[38] L. Hu, K.A. Boateng, J.M. Hill, J. Mol. Catal. A: Chem. 259 (2006) 51–60.
[39] J. Choi, K. Park, I. Park, W. Nam, Y. Sung, Electrochim. Acta 50 (2004) 787–790.
[40] G.W. Graham, T.J. Potter, W.H. Weber, J. Vac. Sci. Technol. A 7 (1989) 1694–1696.
[41] W.D. Westwood, C.D. Bennewitz, J. Appl. Phys. 45 (1974) 2313–2315.
[42] R.J. Berry, Surf. Sci. 76 (1978) 415–442.
[43] H. Hirata, K. Kishita, Y. Nagai, K. Dohnae, H. Shinjoh, S. Matsumoto, Proceeding of the TOCAT6/APCAT5, Sapporo, July 18–23, 2010.
[44] H. Shinjoh, Proceeding of the 6th International Conference on Environmental Catalysis, Beijing, September 12–15, 2010.
[45] M. Ojeda, M.L. Granados, S. Rojas, P. Terreros, F.J. García-García, J.L.G. Fierro, Appl. Catal. A 261 (2004) 47–55.
[46] R. Burch, P.K. Loader, N.A. Cruise, Appl. Catal. A 147 (1996) 375–394.
[47] E.I. Kauppi, R.K. Kaila, J.A. Linnekoski, A.O.I. Krause, M.K. Veringa Niemelä, Int. J. Hydrogen Energy 35 (2010) 7759–7767.
[48] F. Can, A.L. Valant, N. Bion, F. Epron, D. Duprez, J. Phys. Chem. 112 (2008) 14145–14153.
[49] A. Shamsi, J.P. Baltrus, J.J. Spivey, Appl. Catal. A 294 (2005) 145–152.
[50] C. Li, T.C. Brown, Carbon 39 (2001) 725–727.
[51] J.R. Rostrup-Nielsen, T.S. Christensen, I. Dybkjaer, Stud. Surf. Sci. Catal. 113 (1998) 81–95.
[52] S. Yoon, I. Kang, J. Bae, Int. J. Hydrogen Energy 22 (2008) 4780–4788.
[53] S. Nassos, E. Elm Svensson, M. Nilsson, M. Boutonnet, S. Järås, Appl. Catal. B 64 (2006) 96–102.
[54] S. Xu, R. Zhao, Fuel Process. Technol. 86 (2004) 123–133.
[55] C.T. Au, H.Y. Wang, J. Catal. 167 (1997) 337–345.
[56] N.J. Degenstein, R. Subramanian, L.D. Schmidt, Appl. Catal. A 205 (2006) 146–159.
[57] K. Nagaoka, K. Seshan, K. Aika, J.A. Lercher, J. Catal. 197 (2001) 34–42.
[58] D.D. Beck, T.W. Capehart, C. Wong, D.N. Belton, J. Catal. 144 (1993) 311–324.
[59] K. Okumura, S. Hyodo, S. Noda, J. Phys. Chem. B (1998) 2350–2355.
[60] K. Tanaka, Surf. Sci. 357–358 (1996) 721–728.
[61] M. García-Diéguez, E. Finocchio, M.A. Larrubia, L.J. Alemany, G. Busca, J. Catal. 274 (2010) 11–20.
[62] X. Cheng, Z. Shi, N. Glass, L. Zhang, J. Zhang, D. Song, Z.S. Liu, H. Wang, J. Shen, J. Power Sources 165 (2007) 739–756.
[63] A. Suopanki, R. Polvinen, M. Valden, M. Härkönen, Catal. Today 100 (2005) 327.
[64] S. Eriksson, Development of catalysts for natural gas-fired gas turbine combustors, PhD thesis. KTH, Department of Chemical Engineering and Technology, TRITA-KET R232, ISBN:978-91-7178-543-5, 2006.